

Ultrasensitive organic phototransistors with multispectral response based on thin-film/single-crystal bilayer structures

R. M. Pinto,^{1,2, a)} W. Gouveia,¹ A. I. S. Neves,^{1,3} and H. Alves^{1,4}

¹⁾*INESC MN and IN, Rua Alves Redol 9, 1000-029 Lisboa, Portugal*

²⁾*CQFM, Instituto Superior Técnico, Av. Rovisco Pais, 1049-001 Lisboa, Portugal*

³⁾*College of Engineering, Mathematics & Physical Sciences, University of Exeter, EX4 4QL, United Kingdom.*

⁴⁾*CICECO, Physics Department, Universidade de Aveiro, 3810-193 Aveiro, Portugal*

(Dated: 24 September 2015)

We report on highly efficient organic phototransistors (OPTs) based on thin-film/single-crystal planar bilayer junctions between 5,6,11,12-tetraphenyltetracene (rubrene) and [6,6]-phenyl-C₆₁-butyric acid methyl ester (PC₆₁BM). The OPTs show good field-effect characteristics in the dark, with high hole-mobility ($4\text{-}5\text{ cm}^2\text{ V}^{-1}\text{s}^{-1}$), low-contact resistance ($20\text{ k}\Omega\text{-cm}$) and low-operating voltage ($\leq 5\text{ V}$). Excellent sensing capabilities allow for light detection in the 400-750 nm range, with photocurrent/dark current ratio as high as 4×10^4 , responsivity on the order of 20 AW^{-1} at $27\text{ }\mu\text{Wcm}^{-2}$, and an external quantum efficiency of 52 000%. Photocurrent generation is attributed to enhanced electron and hole transfer at the interface between rubrene and PC₆₁BM, and fast response times are observed as a consequence of the high-mobility of the interfaces. The optoelectronic properties exhibited in these OPTs outperform those typically provided by a-Si based devices, enabling future applications where multifunctionality in a single-device is sought.

PACS numbers: 85.60.Dw, 81.05.Fb, 73.50.Pz

^{a)} Author to whom correspondence should be addressed. Email: rpinto@inesc-mn.pt

Field-effect transistors based on organic single-crystals (SCs) have been often used as tools to investigate the intrinsic properties of organic semiconductors, due to the long-range order of the active medium.^{1,2} They can serve as light-sensing optoelectronic devices termed phototransistors (OPTs), if the semiconductor comprising the active channel is photosensitive.³ In recent years, research on OPTs has been active on bringing the best of organic materials, *application-tuned functionality*, to an increasing number of applications, e.g. light-induced switches,⁴ inverters,⁵ memory circuits⁶ and highly sensitive image sensors.⁷ Typically, OPTs are more sensitive than photodiodes, with lower dark-levels, due to their built-in capacity of providing large signal amplification.⁷ Their responsivity (R_{ph}) can be tuned by the voltage applied to source/drain/gate (S/D/G) electrodes.⁶ Unlike photodiodes,⁸ OPTs can reach external quantum efficiencies (EQEs) in excess⁹ of 100%, with spectral coverage depending on the materials used.

To broaden the spectral response and increase charge-separation, heterojunctions (HJs) of donor and acceptor materials have been in used in OPTs.^{4,5} While this strategy is common practice in organic solar cells,^{10,11} its application to OPTs is still limited.⁷ Devices based on solution-processed blends exhibit low charge-mobilities ($10^{-2} \text{ cm}^2\text{V}^{-1}\text{s}^{-1}$), which limit the use of OPTs as regular transistors.⁴ By using single-crystals as active channels, this problem diminishes.³ Yet, until now, SC-based OPTs have been restricted to single-layer architectures, where spectral coverage is limited by the absorption range of the one single material used.^{3,6,7} To this end, further research on OPTs based on SC interfaces and bilayers is of primary importance to the development of high-performance optoelectronic devices.

In this letter we present OPTs with an active layer comprised of single-crystal (SC) rubrene on top of a PC₆₁BM thin-film [Fig. 1]. Such OPTs operate at low-voltage (≤ 5 V), exhibit an average field-effect mobility (μ_{FE}) of $4\text{-}5 \text{ cm}^2\text{V}^{-1}\text{s}^{-1}$, a $I_{\text{ON/OFF}}$ ratio of 10^4 , and a photosensitivity ($P=I_{\text{ph}}/I_{\text{d}}$) of 10^4 . They also show an extended responsivity over the entire visible region (400-750 nm) with external quantum efficiency (EQE) reaching 52 000%.

The fabrication of the interfaces is similar to that reported in our previous work,¹² except that here we use a Si/SiO₂ substrate and a thinner PC₆₁BM layer. Prior to spin-coating a PC₆₁BM solution on top of the substrate, the SiO₂ surface is cleaned by reactive ion etching (RIE) in an oxygen plasma. PC₆₁BM:chlorobenzene solution (20 mg mL^{-1}) is sonicated overnight ($\sim 12\text{h}$, $50 \text{ }^\circ\text{C}$), filtered ($0.2 \text{ }\mu\text{m}$ PTFE) and spin-casted on top of heavily doped

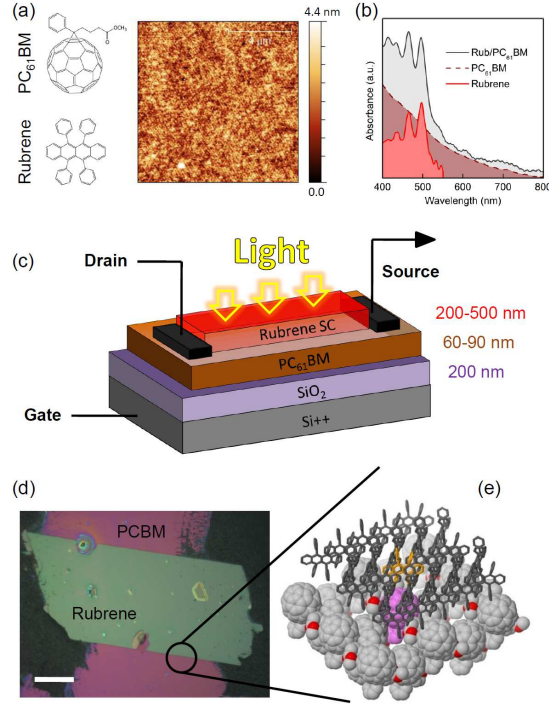


FIG. 1. (a) Chemical structure of PC₆₁BM and rubrene, and AFM image ($10 \times 10 \mu\text{m}^2$) of PC₆₁BM film. (b) Absorption profile of the materials and interface used in this study. (c) Schematic representation of the PC₆₁BM/rubrene OPT. (d) Optical microscope image of the PC₆₁BM film/rubrene single-crystal interface on top of a Si/SiO₂ substrate, with carbon paste as S/D contacts. (e) Molecular view of the organic interface.

n-type Si substrate (5x20 mm) with a thermally grown 200 nm thick SiO₂ layer. The latter two act as gate electrode and gate dielectric, respectively. The substrate was held at room temperature during the coating process, resulting in a smooth PC₆₁BM film (r.m.s. roughness=0.7 nm), as shown in the atomic force microscopy (AFM) image in Fig. 1(a). The thickness of the films was 60-90 nm, measured with a contact surface profilometer. Films were left air-drying in a laminar flow hood for ~ 12 h before the lamination step, to minimize solvent inclusion.

Stripe-like rubrene SCs are grown by physical vapor transport¹³ (PVT), under a stream of high-purity Ar, as reported before.^{12,14} The PVT method overcomes solvent inclusion that plagues most solution-based techniques, while being the most feasible method for obtaining high-purity crystals with perfect lattices. Selected rubrene SCs with length(L)/width(W)

ratio >1 and thickness $t < 500$ nm, were carefully laminated on top of the PC₆₁BM layer. If channel (R_{ch}) and contact (R_{c}) resistances are comparable, then opting for $L/W > 1$ minimizes the negative effect of contact resistance on charge-extraction, since $R_{\text{T}} = R_{\text{ch}} + R_{\text{c}} = R_{\text{s}}(L/W) + R_{\text{c}}$, where R_{T} and R_{s} are total and sheet resistance, respectively. The crystals completely adhere to the surface of the film, guaranteeing the formation of a nanoscale interface [Figs. 1(d)-1(e)]. The structural integrity of rubrene is preserved with lamination, and this results in a hybrid-phase bilayer junction of a crystalline electron-donor layer (rubrene) and an amorphous acceptor layer (PC₆₁BM). S/D contacts are formed using a water-based carbon solution, deposited at the far edges of the interface across the long axis of crystal growth (b -axis). This is the axis of closest π -stacking and highest-mobility in OFETs of single-crystal rubrene.¹ The resulting devices have the same bottom-gate/middle-contact (BG/MC) three-terminal configuration also found in e.g. C₆₀/pentacene OFETs.¹⁵ In our devices, the channel conductance can also be controlled by light irradiation [Fig. 1(c)].

Figures 2(a) and 2(b) present the transfer ($I_{\text{DS}}-V_{\text{GS}}$) and output ($I_{\text{DS}}-V_{\text{DS}}$) characteristics of a representative PC₆₁BM/rubrene OPT ($L=260$ μm , $L/W \sim 1.5$) measured in the dark, under ambient conditions. The current increases with increasing negative gate voltage, typical of field-effect-induced hole conduction. This is the expected behavior for rubrene, meaning that the interface conduction is dominated by unipolar transport in the p -type layer. Unlike PC₆₁BM/pentacene thin-film based OPTs,⁵ we did not observe ambipolar behavior in the PC₆₁BM/rubrene devices. We attribute this to the large mobility unbalance ($\mu_{\text{h}} > 100\mu_{\text{e}}$) arising from the long-range order of the rubrene SC layer, which allows mobilities as high as $10 \text{ cm}^2\text{V}^{-1}\text{s}^{-1}$, in contrast to the low electron mobility observed in PC₆₁BM amorphous thin-film transistors ($10^{-2}\text{cm}^2\text{V}^{-1}\text{s}^{-1}$).^{1,16} Note that achieving ambipolar operation in bilayer/bulk OFETs often requires lower-work function electrodes, and trap passivating layers.⁵ It also implies using higher operating voltages, with fewer available options to create ohmic contacts for effective electron injection, and characterization in oxygen-free environment. None of these strategies were pursued herein.

The mobility and threshold voltage (V_{th}) in the saturation regime ($V_{\text{DS}} > V_{\text{GS}}$) are $4.9 \text{ cm}^2\text{V}^{-1}\text{s}^{-1}$ and 0.59 V, respectively, calculated according to $I_{\text{DS}} = (\mu C_i W / 2L)(V_{\text{GS}} - V_{\text{th}})^2$. In determining μ_{h} , only the capacitance of the SiO₂ layer was considered ($C_i = 17.3 \text{ nF cm}^{-2}$). If the capacitance due to the PCBM layer is added ($\epsilon_r = 3$, $t=100$ nm), the average hole mobility drops to $\approx 40\%$ of the original value, which for the above case leads to ca. 2

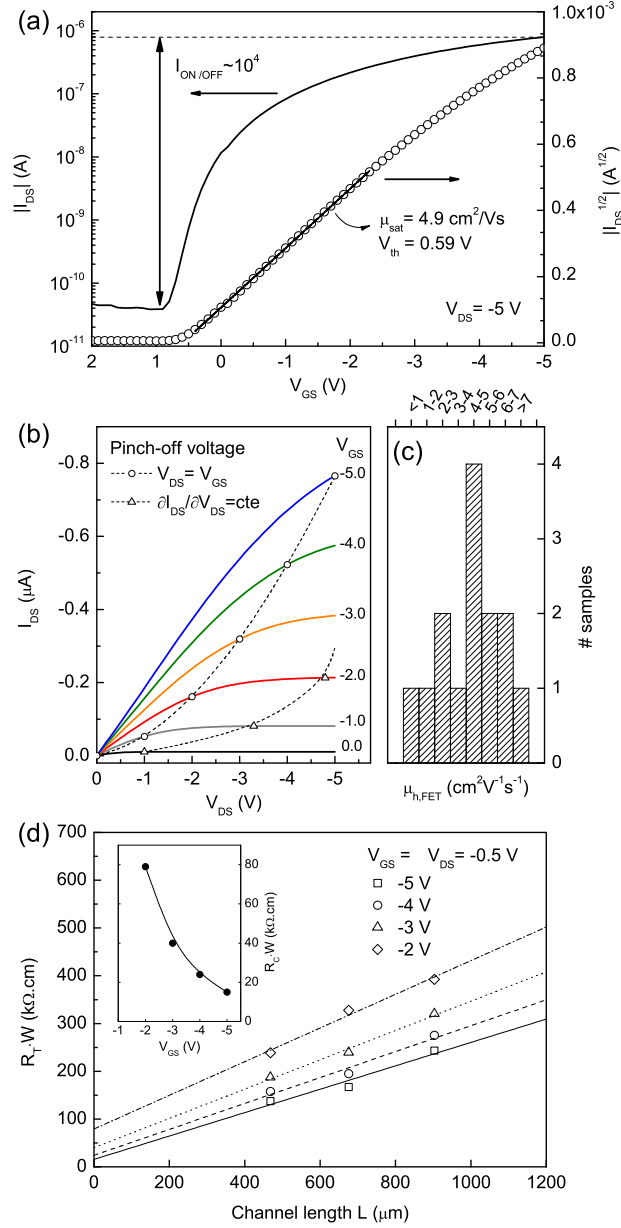


FIG. 2. (a) Transfer and (b) output characteristics measured at different gate voltages, in the dark, of a PC₆₁BM/rubrene OPT with $L \times W = 260 \times 167 \mu\text{m}^2$. (c) Mobility spread for PC₆₁BM/rubrene OPTs measured in the saturation regime. (d) $R_T W$ -L plots for three specific devices, at different V_{GS} , to extract the contact resistance (R_C) in the linear regime via TLM. Inset: contact resistance as a function of V_{GS} .

$\text{cm}^2\text{V}^{-1}\text{s}^{-1}$, still in line with data reported for rubrene single-crystal FETs.

The OPTs exhibit low pinch-off voltages, as estimated by V_{DS} above which $\partial I_{DS}/\partial V_{DS}$

becomes constant [Fig. 2(b)].¹⁷ Hole mobility is $5 \text{ cm}^2\text{V}^{-1}\text{s}^{-1}$, measured in the saturation regime, with average V_{th} of 0.67 V. The 14 devices present some dispersion due to differences in crystal quality [Fig. 2(c)]. The non-zero threshold voltage could be related to the existence of a built-in channel, formed from partial charge-transfer between PC₆₁BM and rubrene,¹² or to a non-negligible density of charge traps present at the active channel/dielectric interface¹⁸. Overall, the performance of these devices as standard OFETs is in line with other systems based on *p*-type organic SCs, such as acenes and tetrathiafulvalene (TTF) derivatives.^{3,18} R_c is $20 \text{ k}\Omega\cdot\text{cm}$, extracted by the transmission line method¹⁹ (TLM) in the linear regime, and gate dependent as presented in Fig. 2(d). Noticeably, this value is of the same order of magnitude as the contact resistance of $5 \text{ k}\Omega\text{cm}$ measured in bottom-gate/top-contact rubrene SC FETs using Au electrodes.²

After demonstration of the high performance of PC₆₁BM/rubrene devices as standard FETs in the dark, we measured their properties operating as sensing elements in the visible-NIR range. OPT performance is analysed based on three figures-of-merit: light responsivity (R_{ph}), photosensitivity (P) and external quantum efficiency (EQE). These parameters enable a normalized comparison between devices. R_{ph} , in AW^{-1} , can be defined by the following equation:⁴

$$R_{\text{ph}} = \frac{I_{\text{ph}}S_{\text{ch}}^{-1}}{E_{\text{light}}} = \frac{(I_1 - I_d)(LxW)^{-1}}{P_{\text{opt}}S_b^{-1}}, \quad (1)$$

where I_{ph} is the source-drain photocurrent, I_1 and I_d are the source-drain current at fixed drain and gate voltages, under light illumination and in the dark, respectively. $E_{\text{light}}=P_{\text{opt}}/S_b$ is the irradiance of the excitation source, where P_{opt} is the optical power and S_b the excitation beam spot size (typically, 1 mm^2). To enable a comparison among devices with crystals of different sizes, I_{ph} is normalized by the active (interface) channel area S_{ch} .

Figure 3(a) shows V_{th} -normalized transfer curves of a PC₆₁BM/rubrene OPT, in the dark and under illumination with a monochromatic green light ($\lambda=500 \text{ nm}$, $E_{\text{light}}\approx 16.8 \mu\text{W mm}^{-2}$). The measurement setup used for optoelectronic characterization of the OPTs is described elsewhere.^{12,20} Light at 500 nm matches the maximum absorption peak of rubrene SC in the visible range [see Fig. 1(a) and Ref.¹²]. Hence, photocurrent build-up in the active channel should originate from rubrene's excitons that split at the interface with PC₆₁BM. The high current increase upon illumination indicates that light can act as an additional terminal that controls device operation, along with the standard S/D and G electrodes. The effect is also observed at other wavelengths in the visible range, as can be seen on Fig. 3(b)

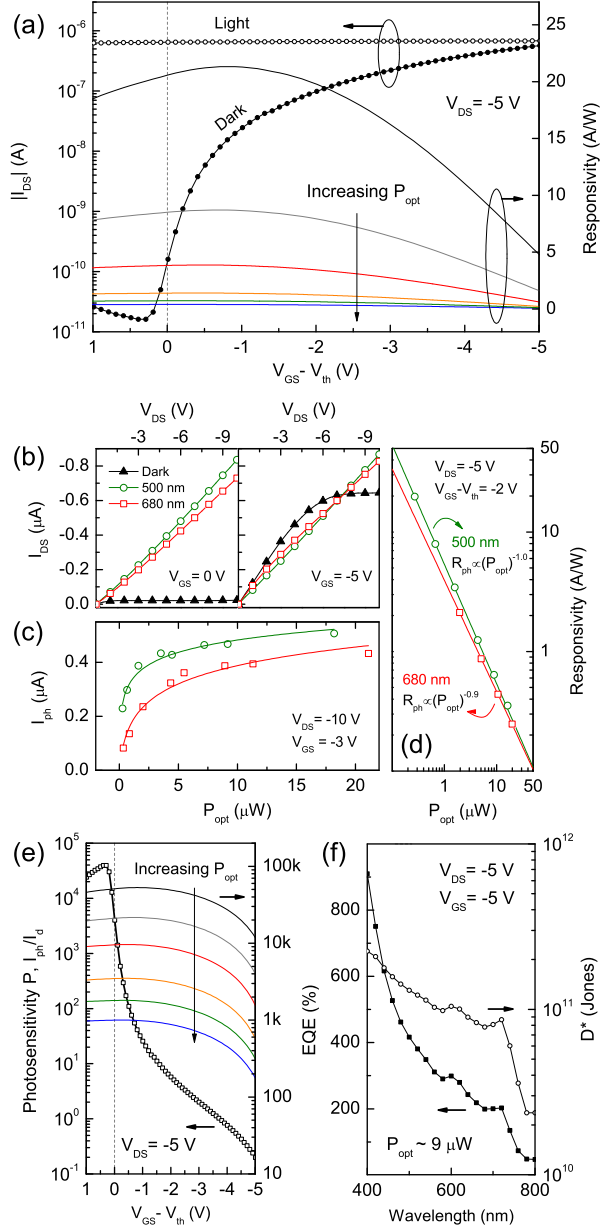


FIG. 3. (a) V_{th} -normalized transfer characteristics of a PC₆₁BM/rubrene OPT ($L \times W = 260 \times 167 \mu\text{m}^2$) measured at $V_{DS} = -5$ V, in the dark, and under green light illumination ($\lambda = 500$ nm, $16.3 \mu\text{W}$). Responsivity R_{ph} as a function $V_{GS} - V_{th}$ with increasing optical power ($P_{opt} = 16.8$ to $0.3 \mu\text{W}$). (b) Drain current in the dark, and under 500 and 680 nm illumination, at $V_{GS} = 0$ and -5 V. (c) Photocurrent and (d) responsivity as a function of P_{opt} . (e) Photosensitivity P as a function of $V_{GS} - V_{th}$, and EQE dependence on gate voltage and P_{opt} . (f) EQE and specific detectivity D^* over 400–800 nm, under strong irradiance ($E_{light} = 0.9 \text{ mWcm}^{-2}$).

with illumination at 680 nm. However, at on-state, the difference between dark and light is less pronounced, and in the saturation regime I_{DS} light levels rise above the dark current. The I_{DS} increase at wavelengths higher than 550 nm is due to PC₆₁BM excitons evolving into free-charges via a hole transfer (HT) mechanism.¹²

When the transistor operates in accumulation mode (on-state, i.e., $V_{GS}-V_{th}<0$ for p -type device), it presents the maximum responsivity, $\approx 20 \text{ AW}^{-1}$, at lowest optical power [Fig.3(a)]. A possible explanation is a photovoltaic (PV) effect, causing a P_{opt} -dependent photocurrent that can be expressed as:²¹

$$I_{ph,pv} = \frac{AkT}{q} \cdot \ln \left(1 + \frac{B\eta q\lambda P_{opt}}{I_d hc} \right), \quad (2)$$

where A and B are fitting parameters, hc/λ is the photon energy, I_d the dark current for electrons, and η the photogeneration quantum efficiency. Fittings to measured data using Eq. 2 show that I_{ph} saturates at high P_{opt} [Fig. 3(c)] values. These results indicate that PC₆₁BM/rubrene OPTs follow the PV effect in the turn-on state, at spectral regions (500 nm vs. 680 nm) where excitons from either p - (rubrene) or n -type (PC₆₁BM) materials contribute to photocurrent. In the PV effect, photogenerated holes flow to the drain electrode, while negative charges accumulate under the source electrode, reducing the barrier height for hole injection and, thus, the contact resistance.²¹ This leads to a positive shift in V_{th} .

At 680 nm, there is a sublinear dependence of R_{ph} on P_{opt} , i.e. $R_{ph} \propto P^{-0.9}$, which likely comes from enhanced singlet-singlet exciton annihilation, due to higher density of photogenerated excitons at increasing optical power [Fig. 3(d)]. The photosensitivity (or photoswitching ratio) for a typical PC₆₁BM/rubrene OPT, defined as $P=I_{ph}/I_d$, peaks at 4×10^4 under 500 nm light illumination, near $V_{GS}-V_{th}=0$ in the off-state of the transistor, as displayed in Fig. 3(e). Similarly to other p -type OPTs, photosensitivity decreases with more negative V_{GS} , owing to the large drain current already flowing through the channel without illumination. Increasing P_{opt} leads to negligible changes in photosensitivity, therefore P is almost independent of light power.

Also in Fig. 3(e), EQE is presented, which takes only into account the electronic processes in the device and is related to R_{ph} as:

$$\text{EQE} = \frac{hc}{\lambda q} R_{ph}. \quad (3)$$

At low irradiance values ($E_{light}=27 \mu\text{Wcm}^{-2}$, 500 nm), EQE reaches 52 900%. Such value is almost 20x higher than the gain observed for high-quality n^+p photodiodes ($>3000\%$).²²

It can be attributed to the existence of a photomultiplication (PM) mechanism, and to the low charge-recombination due to the defect-free nature of rubrene SCs. Under stronger irradiance ($E_{\text{light}}=0.9 \text{ mWcm}^{-2}$), EQE is 900% at 400 nm, and follows the absorption profile of the interface up to ca. 700 nm, decreasing to 200%. It then steeply goes below 50%, signaling the absence of a PM mechanism [Fig. 3(f)]. Note that the onset of the EQE spectrum occurs right at the onset of absorbance for the film/single-crystal interface shown in Fig. 1(b), as observed before.¹² Specific detectivity (D^*) is $1\text{-}2\times 10^{11}$ Jones, calculated using $D^* = R_{\text{ph}}/\sqrt{2eI_{\text{d}}/S_{\text{ch}}}$, where e is the electron charge, R is responsivity, I_{d} the dark current for electrons and S_{ch} is the device area. Shot noise from dark current was assumed as the dominant contribution over Johnson, dielectric or flicker noise.²³

In OPTs, EQEs in excess of 100% can have multiple origins, all relying on some type of PM mechanism, e.g. (i) singlet-fission,²⁴ (ii) impact ionization by hot carriers, or (iii) enhanced injection via trap-assisted tunneling (TAT).^{9,25-27} We rule out the first two, since singlet-fission implies very energetic photons and does not account for the high EQE at lower wavelength, while impact ionization is hampered by the relatively large exciton binding energies of rubrene and PC₆₁BM. However, TAT injection of holes has been observed in P3HT:PC₆₁BM and P3HT:PC₇₁BM photodiodes, leading to EQEs of 37 500% and 84 100% under 625 nm light illumination.^{26,27} Bao and Oh⁹ have also pointed TAT injection as the source of giant EQE (263 000%) in BPE-PTCDI nanowire (NW) phototransistors, where the single-crystalline nature of these NWs provided longer exciton diffusion length (L_{D}) and improved charge-transport. This phenomenon was first reported by Hiramoto's group, for CuPc/Me-PTC photodiodes showing x3000 photocurrent multiplication,²⁵ and has ever since been often used to explain EQEs exceeding 100% in OPTs. Similarly to the PV effect described before, the TAT mechanism also yields a lower injection barrier (i.e. contact resistance). Yet, while the PV effect results from electron accumulation under the source electrode due excess photogenerated electrons confined to a slow mobility layer, the TAT enhanced-injection is uniquely based on the existence of traps near the organic/organic and organic/metal interfaces that bend the energy levels towards lower injection barriers.

Even if actual PM mechanisms are still under debate, a possible explanation for the high EQE in our devices can be described as follows. Starting from illumination in the off-state ($V_{\text{GS}}>0$, $V_{\text{DS}}<0$), photogenerated excitons in rubrene SC diffuse towards the organic/organic interface. There they split driven by an electrical field due to interfacial level bending¹² and

transversal gate-field effect. Holes will drift to the drain, and remnant electrons will fill interfacial traps in the PCBM layer, creating an intrinsic Coulomb field²⁵ that could further enhance exciton splitting. Due to contacts ohmicity that ensure electrical neutrality, more holes will be injected for each (hole collection)–(electron trapping) event until a recombination process occurs. At this stage, the OPT is working as a two-terminal photoconductor device under the influence of a transversal field, and the PM gain is set by the ratio between charge-recombination and hole transit time.⁷

In the on-state ($V_{GS} < 0$, $V_{DS} < 0$), a channel is formed for hole conduction, so after light is absorbed in rubrene, the photogenerated carriers will add to the current already flowing in the channel. The offset between the LUMO levels of rubrene (-2.7 eV) and PC₆₁BM (-3.7 eV) provides deep trap states (≈ 1 eV) at the organic/organic interface²⁷ that lead to narrower tunneling barriers for holes and to a PM effect, as explained above. When only PCBM excitons are created (>550-600 nm), the TAT injection mechanism should also hold, but the lower L_D of PCBM excitons (5 nm) decreases the splitting efficiency, leading to a lower EQE.

The dynamic response of an average mobility OPT ($L \times W = 468 \times 239 \mu\text{m}^2$, $\mu_{FE} = 4.5 \text{ cm}^2\text{V}^{-1}\text{s}^{-1}$) is displayed in Fig. 4(a), showing multispectral photoresponse from 450 to 750 nm, with P as high as 3.1×10^4 when a gate-reset pulse is used. This broad spectral response, which covers the entire visible range and extends into the NIR, is a consequence of enhanced electron (ET) and hole transfer (HT) in the active layer. While this strategy is frequently used to exploit excitons from both organic materials in donor-acceptor ($p-n$) junctions in organic solar cells,²⁸ here we show that it can also be applied to OPTs to achieve multispectral response. A closer look at the photocurrent dynamics reveals fast rise times, $\tau_r < 0.5$ s, and slow single exponential decays, $\tau_d \approx 4.0-5.5$ s [Figs. 4(b)-4(c)]. These values are similar to the corresponding τ_r and τ_d reported for hybrid graphene-quantum dots photodetectors,²³ while τ_r is 10x faster than that of recently developed MoS₂ light sensors.²⁹ They also represent a large improvement over OPTs based on amorphous oxide semiconductors, where persistent photoconductivity (PPC) can last for several hours or days.³⁰ As reported for other OPTs, τ_d can be improved to less than 0.5 s (i.e., the temporal resolution of our setup) by applying a short gate pulse (2s, $V_{GS} = -10$ V) which causes a full release of trapped charge carriers.^{3,23,29} This mode of operation, i.e., off-state plus gate-reset pulse, yields lower dark currents that allow higher detectivity, with D^* of $7-9 \times 10^{12}$ Jones,

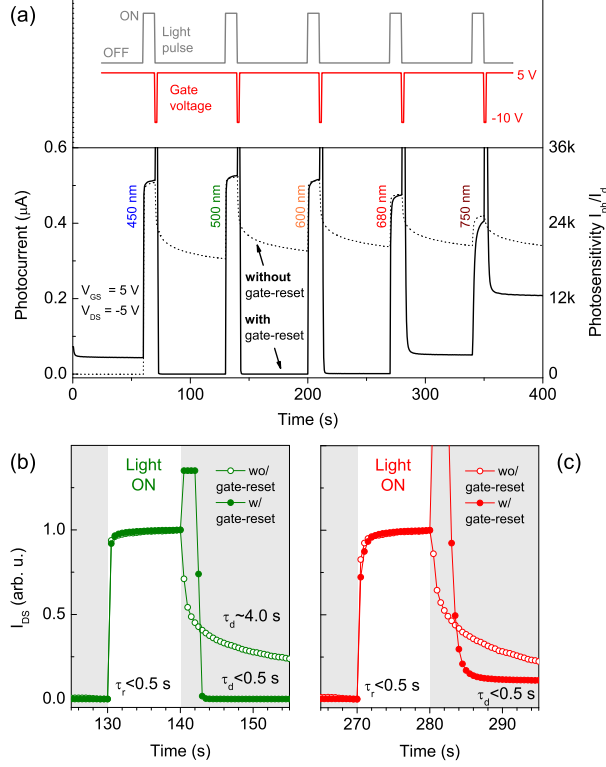


FIG. 4. (a) OPTs photoresponse switching behavior with different excitation wavelengths ($\lambda=450, 500, 600, 680, 750$ nm, $P_{\text{opt}} \approx 7 \mu\text{W}$), in the off-state. A reset voltage pulse, $V_{\text{GS}}=-10$ V, is applied after illumination, during 2 s, to release trapped charge-carriers. Time-resolved photosensitivity with (b) green and (c) red light, showing decay times τ_d of 4.0 and 5.5 s (without gate-reset), and <0.5 s (with gate-reset), respectively, and rise time of τ_r faster than 500 ms.

almost two-orders of magnitude higher than those obtained during on-state operation.

In conclusion, OPTs based on single-crystal rubrene laminated onto PC_{61}BM films show an average hole mobility in the dark of $4\text{-}5 \text{ cm}^2 \text{ V}^{-1}\text{s}^{-1}$, and an EQE that reaches 52 000% under low power light irradiation ($500 \text{ nm}, 27 \mu\text{Wcm}^{-2}$). Response over a wide spectral range (vis-NIR) with photosensitivity P as high as 4×10^4 is achieved by grasping the potential of both p - and n -type materials, whose primary excitons contribute to photocurrent build-up via electron and hole-transfer mechanisms, respectively. These characteristics show the potential of bilayer organic interfaces based on materials with contrasting structural phases (single-crystal vs. amorphous) to be used in high-quality optoelectronic applications.

The authors acknowledge financial support from Fundaço para a Cincia e Tecnologia

(FCT) through contracts SFRH/BPD/84820/2012, IF/01088/2014, and funding through the IN and CICECO Associated Laboratories. A. N. thanks EPSRC for grant EP/M001024/1. The authors thank A. Kholkin (CICECO) for characterizing the PCBM films.

REFERENCES

- ¹E. Menard, V. Podzorov, S.-H. Hur, A. Gaur, M. E. Gershenson, and J. A. Rogers, *Adv. Mater.* **16**, 2097 (2004).
- ²I. N. Hulea, S. Russo, A. Molinari, and A. F. Morpurgo, *Appl. Phys. Lett.* **88**, 113512 (2006).
- ³M. Mas-Torrent, P. Hadley, N. Crivillers, J. Veciana, and C. Rovira, *Chem. Phys. Chem.* **7**, 86 (2006).
- ⁴N. Marjanović, T. B. Singh, G. Dennler, S. Günes, H. Neugebauer, N. Sariciftci, R. Schwödiauer, and S. Bauer, *Org. Electr.* **7**, 188 (2006).
- ⁵J. Labram, P. Wöbkenberg, D. Bradley, and T. Anthopoulos, *Org. Electr.* **11**, 1250 (2010).
- ⁶K. H. Kim, S. Y. Bae, Y. S. Kim, J. A. Hur, M. H. Hoang, T. W. Lee, M. J. Cho, Y. Kim, M. Kim, J.-I. Jin, S.-J. Kim, K. Lee, S. J. Lee, and D. H. Choi, *Adv. Mater.* **23**, 3095 (2011).
- ⁷K.-J. Baeg, M. Binda, D. Natali, M. Caironi, and Y.-Y. Noh, *Adv. Mater.* **25**, 4267 (2013).
- ⁸J. D. Zimmerman, V. V. Diev, K. Hanson, R. R. Lunt, E. K. Yu, M. E. Thompson, and S. R. Forrest, *Adv. Mater.* **22**, 2780 (2010).
- ⁹H. Yu, Z. Bao, and J. H. Oh, *Adv. Funct. Mater.* **23**, 629 (2013).
- ¹⁰F. Yang, M. Shtein, and S. R. Forrest, *Nat. Mater.* **4**, 37 (2005).
- ¹¹W. Ma, C. Yang, X. Gong, K. Lee, and A. J. Heeger, *Adv. Funct. Mater.* **15**, 1617 (2005).
- ¹²R. M. Pinto, E. M. Maçôas, and H. Alves, *J. Mater. Chem. C* **2**, 3639 (2014).
- ¹³R. Laudise, C. Kloc, P. Simpkins, and T. Siegrist, *J. Cryst. Growth* **187**, 449 (1998).
- ¹⁴H. Alves, R. M. Pinto, and E. S. Maçôas, *Nature Commun.* **4**, 1842 (2013).
- ¹⁵E. Kuwahara, Y. Kubozono, T. Hosokawa, T. Nagano, K. Masunari, and A. Fujiwara, *Appl. Phys. Lett.* (2004).
- ¹⁶M. Chikamatsu, S. Nagamatsu, Y. Yoshida, K. Saito, K. Yase, and K. Kikuchi, *Appl. Phys. Lett.* **87**, 3504 (2005).
- ¹⁷M. Imakawa, K. Sawabe, Y. Yomogida, Y. Iwasa, and T. Takenobu, *Appl. Phys. Lett.*

- 99**, 233301 (2011).
- ¹⁸R. de Boer, M. Gershenson, A. Morpurgo, and V. Podzorov, *Phys. Status Solidi A* **201**, 1302 (2004).
- ¹⁹Y. Xu, R. Gwoziecki, I. Chartier, R. Coppard, F. Balestra, and G. Ghibaudo, *Appl. Phys. Lett.* **97**, 063302 (2010).
- ²⁰R. M. Pinto, E. M. S. Macoas, A. I. Neves, S. Raja, C. M. Baleizão, I. C. Santos, and H. Alves, *J. Am. Chem. Soc.* **137**, 7104 (2015).
- ²¹C. Choi, H. Kang, W.-Y. Choi, H. Kim, W. Choi, D. Kim, K. Jang, and K. Seo, *IEEE Photon. Technol. Lett.* **15**, 846 (2003).
- ²²A. J. Said, D. Recht, J. T. Sullivan, J. M. Warrender, T. Buonassisi, P. D. Persans, and M. J. Aziz, *Appl. Phys. Lett.* **99**, 073503 (2011).
- ²³G. Konstantatos, M. Badioli, L. Gaudreau, J. Osmond, M. Bernechea, F. P. G. de Arquer, F. Gatti, and F. H. Koppens, *Nat. Nanotechnol.* **7**, 363 (2012).
- ²⁴D. N. Congreve, J. Lee, N. J. Thompson, E. Hontz, S. R. Yost, P. D. Reuswig, M. E. Bahlke, S. Reineke, T. Van Voorhis, and M. A. Baldo, *Science* **340**, 334 (2013).
- ²⁵M. Hiramoto, K. Nakayama, I. Sato, H. Kumaoka, and M. Yokoyama, *Thin Solid Films* **331**, 71 (1998).
- ²⁶L. Li, F. Zhang, W. Wang, Q. An, J. Wang, Q. Sun, and M. Zhang, *ACS Appl. Mater. Inter.* **7**, 5890 (2015).
- ²⁷W. Wang, F. Zhang, L. Li, M. Zhang, Q. An, J. Wang, and Q. Sun, *J. Mater. Chem. C* **3**, 7386 (2015).
- ²⁸J. D. Douglas, M. S. Chen, J. R. Niskala, O. P. Lee, A. T. Yiu, E. P. Young, and J. M. Fréchet, *Adv. Mater.* **26**, 4313 (2014).
- ²⁹O. Lopez-Sanchez, D. Lembke, M. Kayci, A. Radenovic, and A. Kis, *Nat. Nanotechnol.* **8**, 497 (2013).
- ³⁰S. Jeon, S.-E. Ahn, I. Song, C. J. Kim, U.-I. Chung, E. Lee, I. Yoo, A. Nathan, S. Lee, J. Robertson, *et al.*, *Nat. Mater.* **11**, 301 (2012).